RSC Advances

ROYAL SOCIETY OF CHEMISTRY

PAPER

View Article Online
View Journal | View Issue

Check for updates

Cite this: *RSC Adv.*, 2022, **12**, 26099

Seed layer-free hydrothermal synthesis of porous tungsten trioxide nanoflake arrays for photoelectrochemical water splitting

Yongtao Wang,[a] Xinlei Li[b] and Yuhua Yang*[a]

Received 14th July 2022
Accepted 21st August 2022

DOI: 10.1039/d2ra04313k

rsc.li/rsc-advances

The simple preparation of efficient nano-photoanodes has been a key issue in the development of photoelectrochemical water splitting. In this work, a convenient and seed layer-free hydrothermal approach has been developed to synthesize vertically aligned porous WO_3 nanoflakes on a fluorine-doped tin oxide conductive glass substrate. The morphology of WO_3 nanoflakes could be manipulated by changing the annealing time, which further affected the performance of WO_3 nanoflakes as photoanodes. Under optimum conditions, the obtained photoanode can lead to a high photocurrent density of 2.34 mA cm^{-2} at 1.4 V *vs.* Ag/AgCl under one sun irradiation (100 mW cm^{-2}) and an incident photon to current conversion efficiency of 60% at 300 nm. The excellent photoelectrochemical performance can be mainly attributed to the larger active surface area, single crystal structure with an optimum thickness and the exposed highly active facets.

1. Introduction

Unlike fossil fuels, hydrogen (H_2) is one of the most attractive and environmentally friendly fuels for energy application.[1] Photoelectrochemical (PEC) water splitting is a scalable and cost-effective approach for the generation of H_2, which converts solar energy into chemical energy and stores it in H_2.[2,3] In the PEC reaction, a semiconductor with a suitable band gap is used as the photoelectrode, which can harvest solar energy by absorbing photons and produce photogenerated carriers to realize water splitting.[4–6] Among them, the water reduction reaction for the extraction of H_2 and the water oxidation reaction for the extraction of O_2 occur in the photocathode and photoanode, respectively. Moreover, because the water oxidation reaction is an energetically uphill reaction with the four-electron and four-proton transfer process, the exploration of an efficient photoanode material is key for high performance PEC water splitting. Metal oxides such as TiO_2, ZnO, $BiVO_4$ and WO_3 have been investigated as photoelectrodes owing to their favorable band gap and excellent chemical stability.[7–15] Among them, WO_3 is a prospective photoanode material, which has a higher oxidizing capacity because of its higher valence band potential (3.1–3.2 eV *vs.* NHE),[16,17] suitable bandgap (2.6–2.8 eV),[18] moderate hole diffusion length (~150 nm),[19,20] good electron mobility (~12 cm^2 V^{-1} s^{-1})[21] and low cost. However, although WO_3 possesses impressive advantages as a photoanode material, its practical conversion efficiency is lower than the theoretical value (approximately 10%).[22] The reason is that WO_3 is an indirect bandgap semiconductor, and a relatively thick film is needed for adequate light absorption. However, the thicker WO_3 film usually causes significant recombination of electron–hole pairs.

Compared with the bulk materials, the nanostructured WO_3 photoanode has the advantages of greatly increasing the density of active redox sites, enlarging the semiconductor–electrolyte interface and enhancing the kinetics parameters of the water oxidation reactions through the reduction of bulk recombinations.[22] For example, based on the seed layer-assisted solvothermal growth, Grimes *et al.* synthesized WO_3 nanowire arrays on a fluorine-doped tin oxide (FTO) substrate as a photoanode, which showed the saturation photocurrent of 1.43 mA cm^{-2} under AM 1.5 G illumination.[23] Zhang *et al.* proposed a postgrowth modification method of the WO_3 nanoflakes by a simultaneous solution etching and reducing process, and the modified WO_3 photoanodes showed enhanced PEC performance with a photocurrent density of 1.10 mA cm^{-2} at 1.0 V *vs.* Ag/AgCl.[24] Moreover, Gong *et al.* synthesized the monoclinic multilayered WO_3 photoanode with a photocurrent density of 1.62 mA cm^{-2} at 1.25 V *versus* Ag/AgCl *via* the seed layer-assisted growth.[25] Recently, by employing the 2-step hydrothermal process, Wang *et al.* prepared WO_3 plate-like arrays on a FTO substrate with an unprecedented photocurrent density of 3.7 mA cm^{-2} at 1.23 V *vs.* RHE under AM 1.5 G illumination.[26] However, although great progress in the nanostructured WO_3 photoanode has been made in recent years, the common

---

[a] *Guangzhou Key Laboratory of Flexible Electronic Materials and Wearable Devices, Nanotechnology Research Center, School of Materials Science & Engineering, Sun Yat-Sen University, Guangzhou 510275, China. E-mail: yangyuh3@mail.sysu.edu.cn*

[b] *MOE Key Laboratory of Laser Life Science & Guangdong Provincial Key Laboratory of Laser Life Science, College of Biophotonics, South China Normal University, Guangzhou 510631, China*

synthesis method refers to either the seed layer-assisted growth or multi-step hydrothermal reaction, which is time-consuming and energy-consuming. Moreover, the seed layer containing a large number of nanocrystalline particles can introduce numerous grain boundaries, which eventually results in the increase of interfacial carrier recombination.[27,28] Thus, it is crucial for the development of a simple and seed layer-free synthetic method to grow a nanostructured WO_3 photoanode for PEC water splitting.

Herein, we demonstrate a seed layer-free, one-step hydrothermal synthesis method to grow vertically aligned porous WO_3 nanoflakes on a FTO substrate. The WO_3 nanoflakes comprise a single crystal structure with a thickness of ∼45 nm. The surface morphology and crystalline oriented facets of the WO_3 nanoflakes will evolve with different annealing times. More importantly, the optimal WO_3 nanoflakes exhibit excellent PEC performance without the use of oxygen evolution cocatalysts, which may open up new opportunities in the design of practical photoanodes for PEC water splitting.

2. Experimental

Materials

All chemicals were used without further purification. H_2WO_4 (Sinopharm Chemical Reagent Co., Ltd, GR, ≥99.5%) was used as a tungsten source. H_2O_2 (AR, 30%), HCl (AR, 35%), acetonitrile (AR, ≥99.0%), urea (AR, ≥99.0%), and oxalic acid dihydrate ($H_2C_2O_4 \cdot H_2O$) (AR, ≥99.5%), were used in the precursor solution. The FTO conductive glasses (14 Ω, light transmission rate is 90%) were used as substrates that had been cleaned with acetone, ethanol and deionized water in an ultrasonic bath for 15 min and dried in a nitrogen stream. A Na_2SO_4 solution of 0.1 M (pH 6.8) was used as the electrolyte for testing the photocurrent density, incident-photon-to-current conversion efficiency (IPCE), and the electrochemical impedance spectroscopy (EIS) measurements.

Preparation of the precursor for the hydrothermal reaction

A H_2WO_4 solution as one of the components of the precursor solution was prepared by means of dissolving 1.25 g H_2WO_4 into 20 ml deionized water by adding 20 ml H_2O_2 (30 wt%), which was stirred until it became clear in a hot-water-bath at 95 °C. Then, the H_2WO_4 solution was cooled to room temperature in air. The transparent H_2WO_4 solution was then diluted by deionized water to 100 ml with a molar concentration of 0.05 M. The precursor consists of 3 ml of the above H_2WO_4 solution (0.05 M), 0.15 ml HCl (35%), 0.35 ml deionized water, and 12.5 ml acetonitrile with 0.02 g oxalic acid and 0.02 g urea. Then, the mixture was evenly stirred using a magnetic stirring apparatus until there were no longer solid grains of oxalic acid or urea.

Hydrothermal growth of the WO_3 films

The mixture was placed into a teflon-lined stainless-steel autoclave with a volume of 25 ml. A piece of bare FTO-glass substrate with the conductive layer facing down was immersed and leaned against the wall of the teflon-vessel, which had been previously cleaned. Then, the stainless-steel autoclave was sealed and maintained at 180 °C for 2 h. The as-prepared sample was then rinsed with ethanol and dried in a nitrogen stream. Subsequently, the as-prepared sample was annealed at 500 °C for a certain time in air. In order to study the relationship between the performance and annealing time, the as-prepared samples were annealed for 1 hour, 2 hours and 4 hours in this work, and named as 1 H-WO_3, 2 H-WO_3 and 4 H-WO_3, respectively.

Photoelectrochemical test

The photoelectrochemical (PEC) performance was tested at room temperature by using the typical three-electrode PEC cell with a round flat quartz window. A FTO-glass with the as-prepared samples (1.5 × 1.5 cm^2) was clamped with a Pt electrode holder as the working electrode and a saturated-potassium-chloride silver chloride electrode (Ag/AgCl) as a reference electrode. A platinum foil (1.5 × 1.5 cm^2) as a counter electrode was fixed in the PEC cell with a 0.1 M of Na_2SO_4 solution (pH 6.8). A 300 W Xenon arc lamp (Newport, MODEL 67005) as a light-source simulator provided an illumination intensity of one sun (AM 1.5 G, 100 mW cm^{-2}). The current/potential curves were scanned from −0.2 V to +1.4 V (*vs.* Ag/AgCl @ 25 °C) at a scan rate of 50 mV s^{-1} using an electrochemical station (IVIUM). During the test, the light was vertically illuminated on the working electrode through a quartz window that was parallel with the working electrode and the counter electrode.

In the whole test process, the potential conversion between the Ag/AgCl electrode and reversible hydrogen electrode (RHE) can be expressed by the Nernst equation:

$$E_{\mathrm{RHE}} = E_{\mathrm{Ag/AgCl}} + 0.059\mathrm{PH} + E^0_{\mathrm{Ag/AgCl}}$$

where $E^0_{\mathrm{Ag/AgCl}} = 0.197$ V(@ 25 °C). All of the electrochemical analysis was completed in the Na_2SO_4 solution (pH 6.8) at room temperature, so the equation can be converted to:

$$E_{\mathrm{Ag/AgCl}} = E_{\mathrm{RHE}} - 0.5982$$

IPCE was measured in a Na_2SO_4 solution. A simulator (Newport 69 911 300 W Xenon lamp) coupled to an aligned monochromator (Oriel Cornerstone 260 1/4 m) was used as a simulated light source to provide light at a certain wavelength. A power meter was used to obtain the power density at the certain wavelength, and an electrochemical workstation was used to apply a constant potential (0.63 V *vs.* Ag/AgCl @ 25 °C). IPCE can be expressed as:[29–32]

$$\mathrm{IPCE}(\%) = \frac{J(\mathrm{mA\ \ cm^{-2}}) \times 1240(\mathrm{V\ \ nm})}{\lambda(\mathrm{nm}) \times J_{\mathrm{light}}(\mathrm{nW\ \ cm^{-2}})} \times 100$$

where J is the photocurrent density (mA cm^{-2}) that had been deducted dark current, λ is the incident light wavelength (nm), and J_{light} is the power density measured at a specific wavelength (mW cm^{-2}).

The EIS spectral measurements of the annealed as-prepared samples were performed under an illumination intensity of one sun (AM 1.5 G, 100 mW cm^{-2}) between the frequency of 0.01 Hz to 10 MHz in Na_2SO_4 solution with an AC 0.63 V *vs.* Ag/AgCl bias.

3. Results and discussion

Morphology and characterization

The typical XRD pattern of the unannealed as-prepared sample is given in Fig. 1(a). Peaks marked with an asterisk originate from the FTO substrate. The other diffraction peaks agree well with those of $H_{0.23}WO_3$ with the lattice spacing of $a = 7.546$ Å, $b = 7.546$ Å, $c = 7.546$ Å ($\alpha = 90°$) (PDF#42–1260). The typical SEM of the unannealed as-prepared sample is shown in Fig. 1(b). It can be seen that the nanoflakes vertically grew on the FTO substrate with the uniform thickness of ~45 nm.

After annealing, the XRD pattern of the as-prepared sample changed, as shown in Fig. 2(a). All of the diffraction peaks agree well with those of the monoclinic WO_3 with the lattice spacing of $a = 7.297$ Å, $b = 7.539$ Å, $c = 7.688$ Å ($\alpha = 88.83°$, $\beta = 90.91°$, $\gamma = 90.93°$) (PDF#43-1305). According to the XRD patterns of the three samples, the (002), (020) and (200) planes are exposed in γ-monoclinic WO_3. In addition to the FTO signals, no other peak can be observed, indicating that all samples consisted of pure WO_3. Moreover, the X-ray diffraction peaks become sharper and more intense through increasing the annealed time, which indicated that the 2 H-WO_3 and 4 H-WO_3 samples had better crystallinity than the 1 H-WO_3 sample. The peak of the (002) facets was strengthened with the annealing time increasing from 1 hour to 2 hours, but it almost disappeared when the annealing time was increased to 4 hours. It has been reported that the (002) facets are the most active facets when compared with the other facets of γ-monoclinic WO_3, and have superior activity in the PEC reaction.[25] Therefore, the above results of the XRD patterns suggest that the 2 H-WO_3 sample could be a promising photoanode in PEC water splitting, owing to it having more active facets than the other two as-prepared samples.

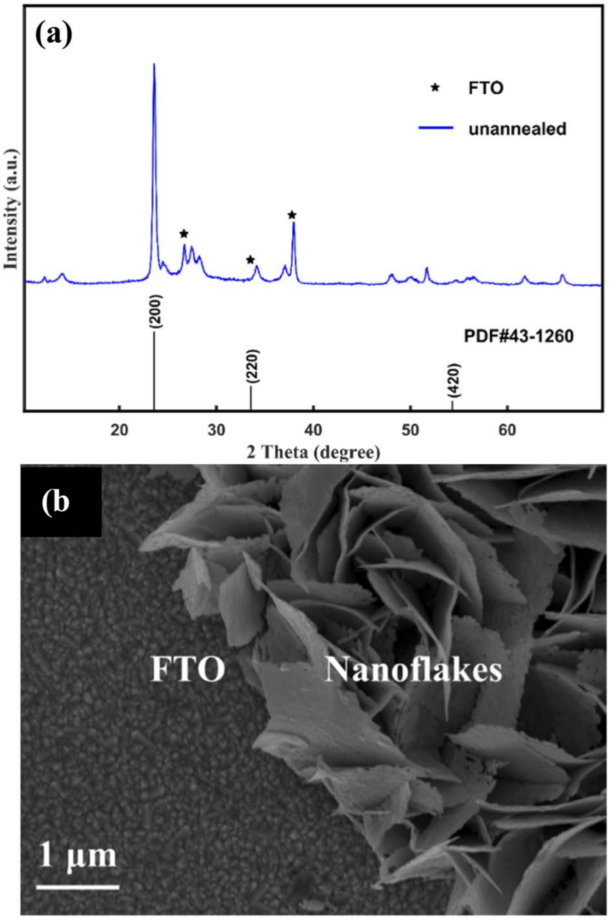

Fig. 1 XRD pattern (a) and SEM image (b) of the unannealed samples. Peaks marked with an asterisk originate from the FTO substrate.

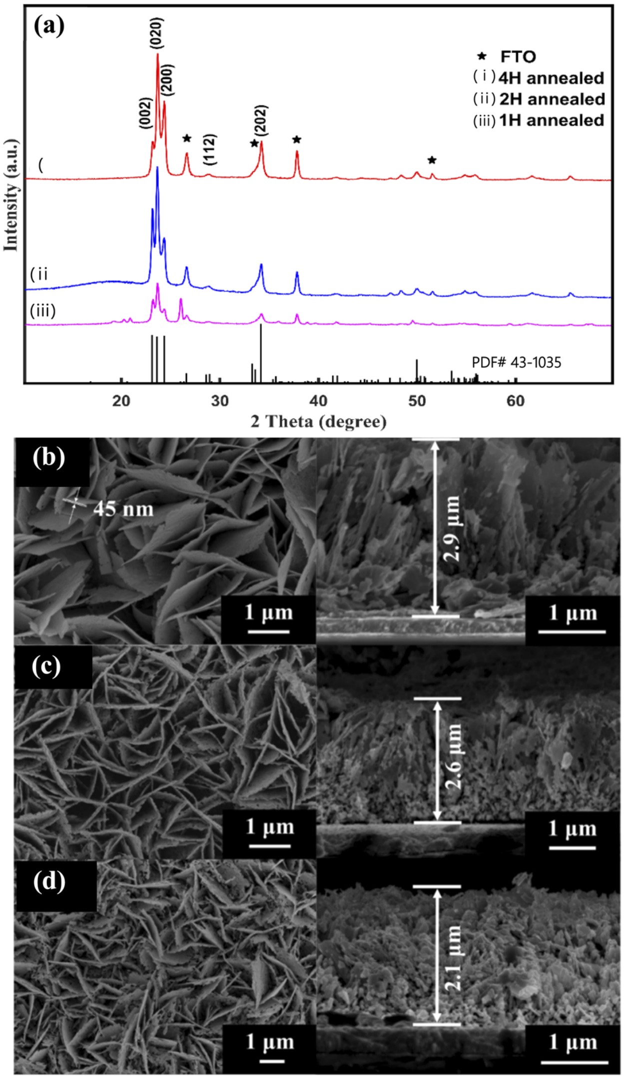

Fig. 2 XRD patterns of the annealed WO_3 nanoflakes (a). SEM images of the WO_3 nanoflakes for different annealed times: (b) 1 hour, (c) 2 hours, (d) 4 hours.

Furthermore, the SEM images revealed that the annealing as-prepared sample is composed of well-aligned WO_3 nanoflakes, as shown in Fig. 2(b–d). The morphology of the nanoflakes is obviously different with different annealing times. The 1 H-WO_3 sample has an intact flake-like morphology, which is the same as that of the as-prepared sample before annealing (Fig. 2(b)). When the annealing time increased to 2 hours, numerous pores were observed in the nanoflakes (Fig. 2(c)). The size and number of the pores increased with increasing annealing time. Furthermore, even the nanoflakes of the 4 H-WO_3 sample were smashed (Fig. 2(d)). The porous structure obtained by annealing is favorable to high PEC performance because the porous structure can afford a higher specific surface area and active sites for electrochemical energy conversion.[33] The thickness of the nanofilms of the 1 H-WO_3, 2 H-WO_3 and 4 H-WO_3 samples also gradually decreased with the annealing time from 2.9 μm to 2.1 μm. Combined with the above XRD results, the crystal transformation may be responsible for the morphological changes of the as-prepared sample *via* annealing in air.[34] The dehydration will result in volume shrinkage, which causes the decrease of the nanofilm thickness and the formation of a porous structure.

Fig. 3 presents the TEM images and SAED patterns of the 2 H-WO_3 nanoflakes. The porous structure was further confirmed by the low-magnification TEM image. The clear SAED patterns reveal that the porous nanoflake is a single crystalline with high crystallinity. Furthermore, the HRTEM image of the nanoflake shows fringe spacings of 0.3764 nm and 0.3838 nm with an angle of 90°, which is consistent with the d-spacing values of the (020) and (002) facets of the monoclinic WO_3, respectively. This excellent single-crystallinity structure of the 2 H-WO_3 nanoflakes can offer direct conduction paths for the photogenerated electrons, which is beneficial for the PEC performance of the sample.[22]

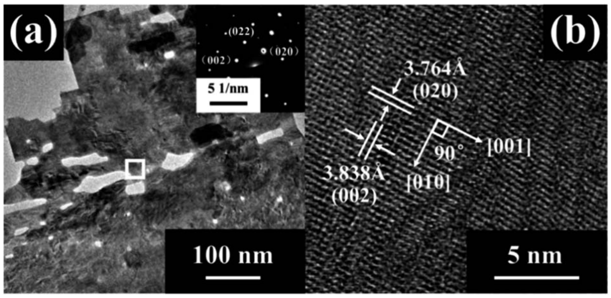

Fig. 3 (a) Low-magnification TEM image of the 2 H-WO_3 nanoflake (the inset shows the corresponding SAED pattern). (b) HRTEM images of the 2 H-WO_3 nanoflake taken from the area marked by a white square in (a).

Photoelectrochemical properties

The PEC performances of the WO_3 nanoflakes electrode were investigated using linear sweep voltammetry conducted from −0.2 to +1.4 V *vs.* Ag/AgCl in a Na_2SO_4 solution (pH 6.8) at room temperature. Fig. 4(a) shows the current density *vs.* potential (*I–V*) curves of 1 H-WO_3, 2 H-WO_3 and 4 H-WO_3. As expected, the 2 H-WO_3 sample exhibits the best PEC performance with the photocurrent density of 2.34 mA cm^{-2} at 1.4 V *vs.* Ag/AgCl at room temperature. Meanwhile, the 1 H-WO_3 and 4 H-WO_3 samples only could reach to 1.65 mA cm^{-2} and 1.54 mA cm^{-2} at the same potential, respectively. Compared with the other reported works,[22–25] our WO_3 nanoflakes synthesized by simple seed layer-free and one-step hydrothermal method have comparable or even better photocurrent density than the other nanostructured WO_3 synthesized by other complex methods. Here, the morphology of the as-prepared sample is suggested to have an important impact on the overall PEC performance. As to the 2H-WO_3 sample, it is a porous structure and more pores exist in the nanoflakes, which can afford higher specific surface area and more reactive active sites for electrochemical energy conversion. The well-aligned WO_3 nanoflakes facilitate the random reflection of light in the array, which further promotes the absorption of solar energy. As to the 1H-WO_3 sample, there are fewer pores in it, so it has fewer reactive active sites compared to the 2H-WO_3 samples. For the 4H-WO_3 sample, due to the long annealing time, its structure was smashed and collapsed. The flakes appeared to be damaged, and then its PEC performance was weakened. In addition, the more active facet (002) of the 2H-WO_3 samples plays a crucial role in its excellent PEC performance.

To obtain a quantitative correlation of the nanoflakes, we performed IPCE measurements as a means of studying the photoactive wavelength regime for the nanostructured WO_3 films. As shown in Fig. 4(b), the IPCE results of the three types of films were consistent with the *I–V* curves, with the 2 H-WO_3 sample giving the highest efficiency value. At 300 nm, the 2 H-WO_3 sample gave IPCE values higher than 60%. However, the 1 H-WO_3 and 4 H-WO_3 samples gave IPCE values of about 48% and 24%, respectively. The data reveal that the 2 H-WO_3 sample had the most outstanding conversion efficiency.

To further explore the origin of the excellent photocatalytic activity, the light absorption of the WO_3 nanoflakes photoanodes was investigated, as shown in Fig. 4(c). The absorption edges of 1 H-WO_3, 2 H-WO_3 and 4 H-WO_3 are located at 340 nm, 380 nm and 360 nm, respectively. The 2 H-WO_3 sample had higher light absorption intensities compared to the other two samples, which indicates the superior PEC efficiency. The optical band gap, *Eg*, can be estimated using the following equation:[35]

$$\alpha hv = A(hv - E_g)^n$$

where h is Planck's constant, v is the frequency of light, A is a constant, and n is equal to 2 for an indirect semiconductor or 1/2 for a direct semiconductor. For WO_3, the transition is indirect. Therefore, $(\alpha hv)^{1/2}$ is plotted as a function of hv, from which the band gap energy is obtained. The E_g values of 1 H-WO_3, 2 H-WO_3 and 4 H-WO_3 were calculated to be 2.90, 2.80 and 2.87 eV, respectively. Combined with the SEM images as shown in Fig. 2, after annealing for 2 hours, more pores were generated in the nanoflakes. Many defects were also introduced in the structures. The shallower defect level in the band structure extended the spectral response region of its photocatalytic activity to a certain extent, which further promoted the absorption of solar energy and improved its photocatalytic efficiency. After annealing for 4 hours, the structures of the 4H-WO_3 nanoflakes were smashed and collapsed. The poor crystal quality led to the degradation of its optical absorption performance, which resulted in the weaker PEC efficiency.

The EIS Nyquist curves of the samples consist of two semicircles and a line, which are assigned to the electrochemical reaction at the Pt counter electrode at high frequencies (R_{ct1}), charge transfer at the WO_3/electrolyte interface at medium frequencies (R_{ct2}), and the Warburg diffusion process of the electrolyte at low frequencies (Z_w).[36] As shown in Fig. 4(d), the arc radii of the three samples at high frequencies are similar, which means they have the same electrochemical reaction at the Pt counter electrode. However, 2 H-WO_3 has the smallest arc radius at medium frequencies, indicating a faster interfacial change transfer and a more effective separation of the photogenerated electron–hole pairs during light illumination.[37] The result clearly demonstrates that the 2 H-WO_3 photoanode with a modest pore density and more exposure of the (002) and (020) facets remarkably increases the electron mobility by reducing the recombination of electron–hole pairs, which results in a higher reaction efficiency.

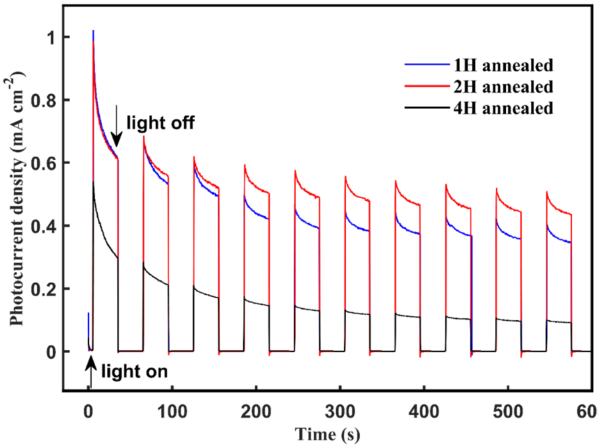

Fig. 5 Photocurrent density *vs.* time curves of the annealing WO_3 nanoflakes at 0.63 V *vs.* Ag/AgCl bias in the Na_2SO_4 solution under AM 1.5 G illumination at room temperature.

Finally, the photocurrent–time curves were measured using the typical three-electrode PEC cell at 0.63 V *vs.* Ag/AgCl in a Na_2SO_4 solution (pH 6.8) under AM 1.5 G illumination for 600 s. The 4 H-WO_3 and 1 H-WO_3 samples exhibit poor stability, and the initial photocurrent density eventually decreased by 83% and 66%, respectively. The photocurrent density of the 2 H-

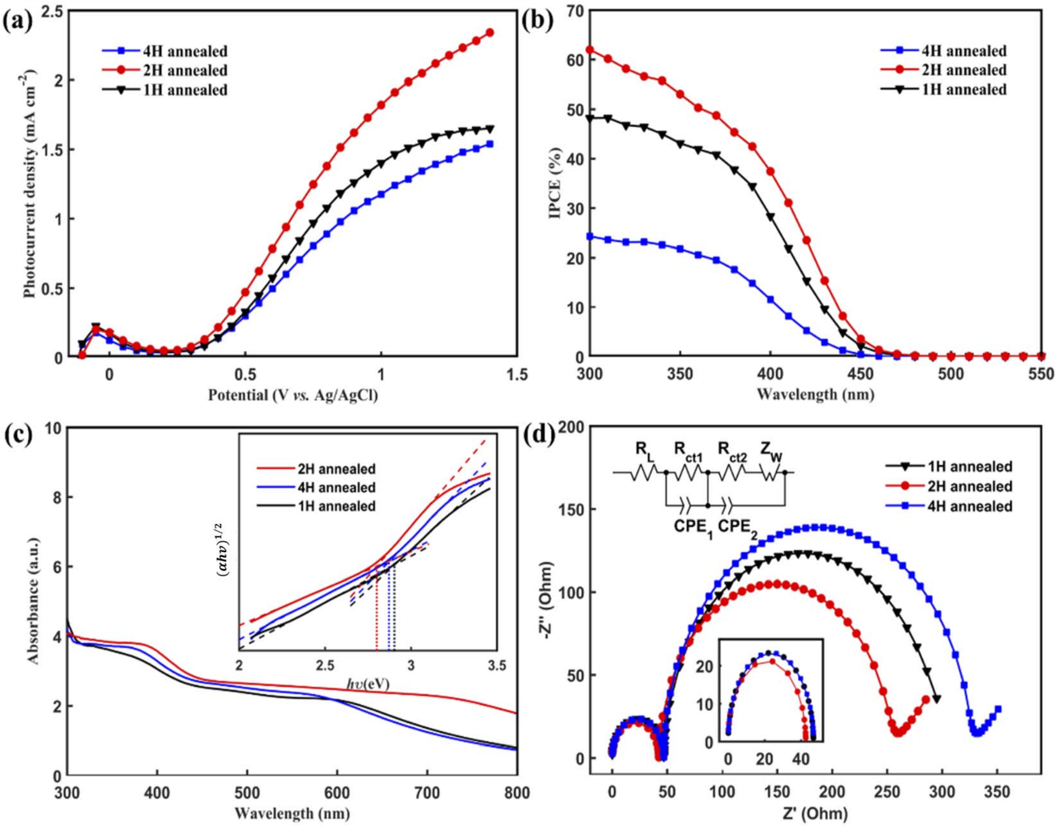

Fig. 4 (a) Current density *vs.* potential (*I*/*V*) curves of the photoelectrodes prepared in a Na_2SO_4 solution were scanned from −0.2 V to +1.4 V (*vs.* Ag/AgCl @ 25 °C) with a scan rate of 50 mV s^{-1} using linear sweep voltammetry. (b) Incident-photon-to-current efficiency (IPCE) *vs.* wavelength curves were collected at 0.63 V (*vs.* Ag/AgCl @ 25 °C) in Na_2SO_4 solution. (c) UV-visible absorption spectra of the WO_3 samples (the inset show the Tauc curves converted from the UV-vis absorption spectra). (d) Electrochemical impedance spectroscopy (EIS) Nyquist curves using a typical three-electrode PEC cell (@ 0.63 V *vs.* Ag/AgCl bias) under AM 1.5 G illumination in the Na_2SO_4 solution at room temperature (the inset show the equivalent and magnification magnifying profile of the EIS curves).

WO_3 sample only decreased by 56% for the initial value, and the enhanced stability can be attributed to the good crystallinity and stable crystal exposed facet.[21] Fig. 5 shows that all photocurrent densities had a rapid jump between zero and saturation values following the light being switched on and off, which indicates that all samples had an efficient charge separation, migration and surface reaction, *i.e.*, high sensitivity.

4. Conclusion

The vertically aligned porous WO_3 nanoflakes have been synthesized by a convenient and seed layer-free hydrothermal approach. The morphology and crystal facet can be manipulated by adjusting the annealing time. The sample with 2 hours annealing time exhibited much better PEC performance, which shows an enhanced photocurrent density of 2.34 mA cm^{-2} at 1.4 V *vs.* Ag/AgCl under AM 1.5 G light irradiation and an IPCE value of more than 60% at 300 nm wavelength without the use of any cocatalyst. The synergistic effect of the porous morphology, good crystallinity and the exposure of high activity (002) facets obtained under 2 hours annealing process effectively enhances the charge transfer efficiency, thereby improving the PEC performance with better photostability.

Conflicts of interest

There are no conflicts of interest to declare.

Acknowledgements

The authors thank the National Natural Science Foundation of China (51002192) and the Open fund of the Guangdong Provincial Key Laboratory of Laser Life Science.

References

1 Y. Li and J. Z. Zhang, Hydrogen Generation from Photoelectrochemical Water Splitting based on Nanomaterials, *Laser Photonics Rev.*, 2010, **4**, 517–528.

2 F. E. Osterloh, Inorganic Nanostructures for Photoelectrochemical and Photocatalytic Water Splitting, *Chem. Soc. Rev.*, 2013, **42**, 2294–2320.

3 P. Zhang, J. J. Zhang and J. L. Gong, Chem. Tantalum-Based Semiconductors for Solar Water Splitting, *Soc. Rev.*, 2014, **43**, 4395–4422.

4 R. E. Blankenship, *et al.*, Comparing Photosynthetic and Photovoltaic Efficiencies and Recognizing the Potential for Improvement, *Science*, 2011, **332**, 805–809.

5 A. Z. Weber, C. X. Xiang, A. Berger, J. Newman, M. Singh, K. Fountaine, J. Stevens, K. Chen, N. Lewis and S. Hu, II.G.20 Joint Center for Artificial Photosynthesis: Modeling and Simulation Team, *Energy Environ. Sci.*, 2013, **6**, 2984.

6 Q. Wang, *et al*, Scalable Water Splitting on Particulate Photocatalyst Sheets with a Solar-to-Hydrogen Energy Conversion Efficiency Exceeding 1, *Nat. Mater.*, 2016, **15**, 611–615.

7 M. D. Batt and J. S. Lee, Recent theoretical progress in the development of photoanode materials for solar water splitting photoelectrochemical cells, *J. Mater. Chem.*, 2015, **3**, 10632–10659.

8 D. K. Lee, D. Lee, M. A. Lumley and K.-S. Choi, Progress on ternary oxide-based photoanodes for use in photoelectrochemical cells for solar water splitting, *Chem. Soc. Rev.*, 2019, **48**, 2126–2157.

9 Y. X. Wang, D. M. Chen, J. N. Zhang, M. S. Balogun, P. S. Wang, Y. X. Tong and Y. C. Huang, Charge relays *via* dual carbon-actions on nanostructured BiVO4 for high performance photoelectrochemical water splitting, *Adv. Funct. Mater.*, 2022, **32**, 2112738.

10 Y. Y. Wang, J. N. Zhang, M.-S. Balogun, Y. X. Tong and Y. C. Huang, Oxygen vacancy-based metal oxides photoanodes in photoelectrochemical water splitting, *Materials Today Sustainability*, 2022, **18**, 100118.

11 X. Y. Lu, K. H. Ye, S. Q. Zhang, J. N. Zhang, J. D. Yang, Y. C. Huang and H. B. Ji, Amorphous type FeOOH modified defective BiVO4 photoanodes for photoelectrochemical water oxidation, *Chem. Eng. J.*, 2022, **428**, 131027.

12 J. N. Zhang, Y. C. Huang, X. Y. Lu, J. D. Yang and Y. X. Tong, Enhanced BiVO4 photoanode photoelectrochemical performance *via* Vorate treatment and a NiFeOx cocatalyst, *ACS Sustainable Chem. Eng.*, 2021, **9**, 8306–8314.

13 M. A. Butler, Photoelectrolysis and Physical Properties of the Semiconducting Electrode WO_3, *J. Appl. Phys.*, 1977, **48**, 1914–1920.

14 W. Morales, M. Cason, O. Aina, N. R. de Tacconi and K. Rajeshwar, Combustion Synthesis and Characterization of Nanocrystalline WO_3, *J. Am. Chem. Soc.*, 2008, **130**, 6318–6319.

15 G. Hodes, D. Cahen and J. Manassen, Tungsten Trioxide as a Photoanode for a Photoelectrochemical cell (PEC), *Nature*, 1976, **260**, 312–313.

16 Q. X. Mi, A. Zhanaidarove, B. S. Brunschwig, H. B. Gray and N. S. Lewis, A Quantitative Assessment of the Competition between Water and Anion Oxidation at WO_3 Photoanodes in Acidic Aqueous Electrolytes, *Energy Environ. Sci.*, 2012, **5**, 5694–5700.

17 M. Miyauchi, Photocatalysis and Photoinduced Hydrophilicity of WO_3 Thin Films with Underlying Pt Nanoparticles, *Phys. Chem. Chem. Phys.*, 2008, **10**, 6258–6265.

18 C. Santato, M. Ulmann and J. Augustynski, Photoelectrochemical Properties of Nanostructured Tungsten Trioxide Films, *J. Phys. Chem. B*, 2001, **105**, 936–940.

19 J. Y. Zheng, Z. Haider, T. K. Van, A. U. Pawer, M. J. Kang, C. W. Kim and Y. S. Kang, Tuning of the Crystal Engineering and Photoelectrochemical Properties of Crystalline Tungsten Oxide for Optoelectronic Device Applications, *CrystEngComm*, 2015, **17**, 6070–6093.

20 F. F. Abdi, T. J. Savenije, M. M. May, B. Dam and R. van de Krol, The Origin of Slow Carrier Transport in BiVO4 Thin

Film Photoanodes: A Time-Resolved Microwave Conductivity Study, *J. Phys. Chem. Lett.*, 2013, **4**, 2752–2757.

21 C. A. Bignozzi, S. Caramori, V. Cristino, R. Argazzi, L. Meda and A. Tacca, Nanostructured Photoelectrodes Based on WO_3: Applications to Photooxidation of Aqueous Electrolytes, *Chem. Soc. Rev.*, 2013, **42**, 2228–2246.

22 M. Park, *et al.*, Enhanced Visible Light Activity of Single-Crystalline WO_3 Microplates for Photoelectrochemical Water Oxidation, *J. Phys. Chem. C*, 2016, **120**, 9192–9199.

23 J. Z. Su, X. J. Feng, J. D. Sloppy, J. L. Guo and C. A. Grimes, Vertically Aligned WO_3 Nanowire Arrays Grown Directly on Transparent Conducting Oxide Coated Glass: Synthesis and Photoelectrochemical Properties, *Nano Lett.*, 2011, **11**, 203–208.

24 W. J. Li, P. Da, Y. Y. Zhang, Y. C. Wang, X. Lin, X. Gong and G. F. Zheng, WO_3 Nanoflakes for Enhanced Photoelectrochemical Conversion, *ACS Nano*, 2014, **8**, 11770–11777.

25 J. J. Zhang, P. Zhang, T. Wang and L. J. Gong, Monoclinic WO_3 Nanomultilayers with Preferentially Exposed (002) Facets for Photoelectrochemical Water Splitting, *Nano Energy*, 2015, **11**, 189–195.

26 S. C. Wang, H. J. Chen, G. P. Gao, T. Butburee, M. Lyu, S. Thaweesak, J.-H. Yun, A. J. Du, G. Liu and L. Z. Wang, Synergistic Crystal Facet Engineering and Structural Control of WO_3 Films Exhibiting unprecedented Photoelectrochemical Performance, *Nano Energy*, 2016, **24**, 94–102.

27 D.-D. Qin, C.-L. Tao, S.-I. In, Z.-Y. Yang, T. E. Mallouk, N. Bao and C. A. Grimes, Facile Solvothermal Method for Fabricating Arrays of Vertically Oriented α-Fe_2O_3 Nanowires and Their Application in Photoelectrochemical Water Oxidation, *Energy Fuels*, 2011, **25**, 5257–5263.

28 F. Amano, D. Li and B. Ohtani, Fabrication and Photoelectrochemical Property of Tungsten(VI) Oxide Films with a Flake-Wall Structure, *Chem. Commun.*, 2010, **46**, 2769–2771.

29 Z. B. Chen, T. F. Jaramillo, T. G. Deutsch, A. Kleiman-Shwarsctein, A. J. Forman, N. Gaillard, R. Garland, K. Takanabe, C. Heske, M. Sunkara, K. McFarland, E. W. Domen, E. L. Miller, J. A. Turner and H. N. Dinh, Accelerating materials development for photoelectrochemical hydrogen production: Standards for methods, definitions, and reporting protocols, *J. Mater. Res.*, 2010, **25**, 3–16.

30 J. Zhang, J. H. Bang, C. Tang and P. V. Kamat, Tailored TiO_2-$SrTiO_3$ Heterostructure Nanotube Arrays for Improved Photoelectrochemical Performance, *ACS Nano*, 2010, **4**, 387–395.

31 S. Hoang, S. W. Guo, N. T. Hahn, A. J. Bard and C. B. Mullins, Visible Light Driven Photoelectrochemical Water Oxidation on Nitrogen-Modified TiO_2 Nanowires, *Nano Lett.*, 2012, **12**, 26–32.

32 Y. H. Ling, G. M. Wang, D. A. Wheeler, J. Z. Zhang and Y. Li, Sn-Doped Hematite Nanostructures for Photoelectrochemical Water Splitting, *Nano Lett.*, 2011, **11**, 2119–2125.

33 B. W. Ren, D. Q. Li, Q. Y. Jin, H. Cui and C. X. Wang, Novel Porous Tungsten Carbide Hybrid Nanowires on Carbon Cloth for High-Performance Hydrogen Evolution, *J. Mater. Chem. A*, 2017, **5**, 13196–13203.

34 J. Yang, W. Z. Li, J. Li, D. B. Sun and Q. Y. Chen, Hydrothermal Synthesis and Photoelectrochemical Properties of Vertically Aligned Tungsten Trioxide (hydrate) Plate-like Arrays Fabricated Directly on FTO Substrates, *J. Mater. Chem.*, 2012, **22**, 17744–17752.

35 J. Tauc, R. Grigorovici and A. Vancu, Optical Properties and Electronic Structure of Amorphous Germanium, *Phys. Status Solidi*, 1966, **15**, 627–637.

36 Y. Bai, H. Yu, Z. Li, R. Amal, G. Q. Lu and L. Z. Wang, In Situ Growth of a ZnO Nanowire Network within a TiO2 Nanoparticle Film for Enhanced Dye-Sensitized Solar Cell Performance, *Adv. Mater.*, 2012, **24**, 5850–5856.

37 M. X. Li, W. J. Luo, D. P. Cao, X. Zhao, Z. S. Li, T. Yu and Z. G. Zou, A Co-catalyst-Loaded Ta3N5 Photoanode with a High Solar Photocurrent for Water Splitting upon Facile Removal of the Surface Layer, *Angew. Chem., Int. Ed. Engl.*, 2013, **52**, 11016–11020.